

Article

# A method to prolong lithium-ion battery life during the full life cycle

Jiangong Zhu, Wentao Xu, Michael Knapp, ..., Haifeng Dai, Xuezhe Wei, Helmut Ehrenberg

zhujiangong@tongji.edu.cn (J.Z.)  
tongjidai@tongji.edu.cn (H.D.)

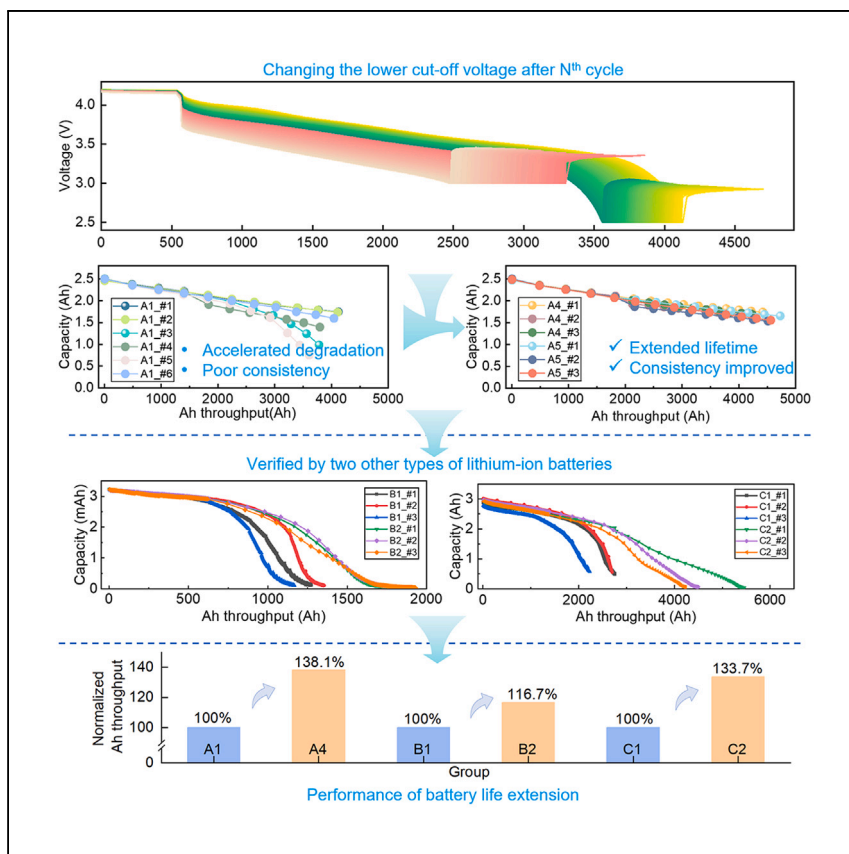
Highlights

Nonlinear and inconsistent degradation is found for lithium-ion batteries

Electrochemical analysis and multiscale postmortem analysis are performed

Raising the cutoff voltage before nonlinear degradation prolongs the battery life

Extension of the cycle lifetime is verified on different battery types



Zhu et al. propose a method for extending the cycle lifetime of lithium-ion batteries by raising the lower cutoff voltage to 3 V when the battery reaches a capacity degradation threshold. This method is shown to increase the cycle lifetime by 16.7%–38.1% for three different types of lithium-ion batteries.



## Article

## A method to prolong lithium-ion battery life during the full life cycle

Jiangong Zhu,<sup>1,2,5,\*</sup> Wentao Xu,<sup>1</sup> Michael Knapp,<sup>2</sup> Mariyam Susana Dewi Darma,<sup>2,3</sup> Liuda Mereacre,<sup>2</sup> Peiji Su,<sup>2</sup> Weibo Hua,<sup>2,4</sup> Xinyang Liu-Théato,<sup>2</sup> Haifeng Dai,<sup>1,\*</sup> Xuezhe Wei,<sup>1</sup> and Helmut Ehrenberg<sup>2,3</sup>

## SUMMARY

Extended lifetime of lithium-ion batteries decreases economic costs and environmental burdens in achieving sustainable development. Cycle life tests are conducted on 18650-type commercial batteries, exhibiting nonlinear and inconsistent degradation. The accelerated fade dispersion is proposed to be triggered by the evolution of an additional potential of the anode during cycling as measured vs.  $\text{Li}^+/\text{Li}$ . A method to prolong the battery cycle lifetime is proposed, in which the lower cutoff voltage is raised to 3 V when the battery reaches a capacity degradation threshold. The results demonstrate a 38.1% increase in throughput at 70% of their beginning of life (BoL) capacity. The method is applied to two other types of lithium-ion batteries. A cycle lifetime extension of 16.7% and 33.7% is achieved at 70% of their BoL capacity, respectively. The proposed method enables lithium-ion batteries to provide long service time, cost savings, and environmental relief while facilitating suitable second-use applications.

## INTRODUCTION

Lithium-ion batteries are unquestionably one of the most promising energy storage components used in electrically operated devices due to their power and energy capabilities, and batteries with long lifetimes are crucial in reducing the negative environmental impact.<sup>1–3</sup> Nevertheless, lithium-ion batteries undergo irreversible aging and fatigue due to their electrochemical nature, which is influenced by cell chemistries (active material, electrolyte, additive, etc.), cell design (cell architecture, electrode engineering, etc.), operation conditions, and use patterns.<sup>4,5</sup>

Long-life battery materials and battery designs have always been pursued, and battery lifespan managements receive increased attention,<sup>6</sup> as extending battery lifetime decreases costs and environmental burdens in achieving sustainable development.<sup>7,8</sup> Large numbers of battery materials have been investigated to improve the cycling stability of active material to achieve long-life batteries.<sup>9</sup> Un-Hyuck Kim et al.<sup>10</sup> introduced a  $\text{Li}[\text{Ni}_{0.90}\text{Co}_{0.09}\text{Ta}_{0.01}]\text{O}_2$  cathode, which exhibited reasonable cycling stability by radially aligned primary particles with [003] crystallographic texture that effectively dissipated the internal strain occurring in the deeply charged state. Odziomek et al.<sup>11</sup> prepared hierarchically structured  $\text{Li}_4\text{Ti}_5\text{O}_{12}$  yielding nano- and microstructure anodes for long life at ultrafast charging, which was verified by cycling tests in half-cells. In addition, battery design is an effective approach to extending battery life. Manikandan Palanisamy et al.<sup>12</sup> investigated the synchronized lithium and lithium-ion batteries containing a thin lithium reservoir-electrode to mitigate the lithium and capacity loss during the formation cycle, which enhanced

<sup>1</sup>Clean Energy Automotive Engineering Center, School of Automotive Engineering, Tongji University, Shanghai 201804, China

<sup>2</sup>Institute for Applied Materials (IAM), Karlsruhe Institute of Technology (KIT), 76344 Eggenstein-Leopoldshafen, Germany

<sup>3</sup>Helmholtz Institute Ulm (HIU) Electrochemical Energy Storage, Helmholtz Strasse 11, 89081 Ulm, Germany

<sup>4</sup>School of Chemical Engineering and Technology, Xi'an Jiaotong University, Xi'an, Shaanxi 710049 China

<sup>5</sup>Lead contact

\*Correspondence: [zhujiangong@tongji.edu.cn](mailto:zhujiangong@tongji.edu.cn) (J.Z.), [tongjidai@tongji.edu.cn](mailto:tongjidai@tongji.edu.cn) (H.D.)

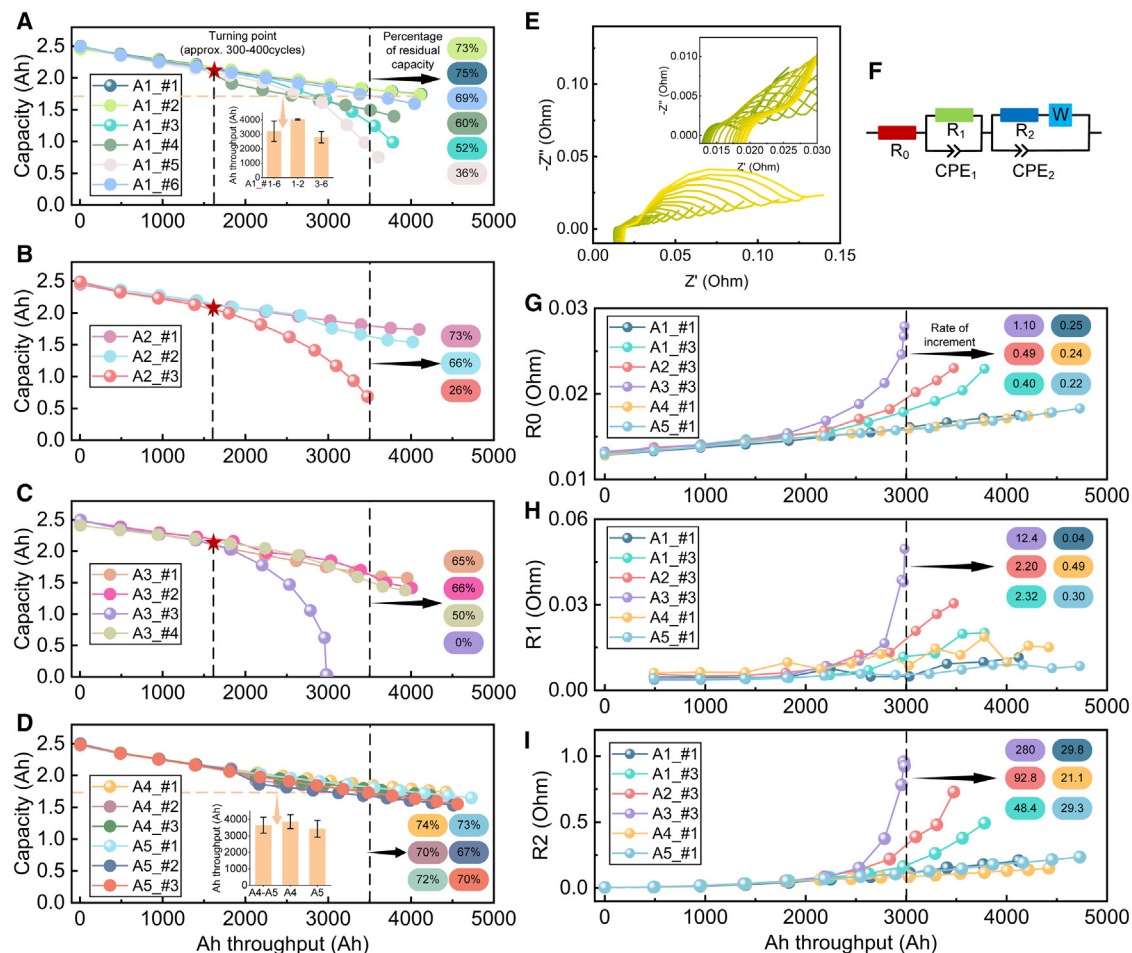
<https://doi.org/10.1016/j.xcrp.2023.101464>



battery life. Wang et al.<sup>13</sup> designed an asymmetric temperature modulation battery with an embedded Ni foil for self-heating to achieve a stable lifetime under fast charging operation.

Battery management, different from the battery material and design improvements, is an applicable way to achieve battery life extension by controlling the state-of-the-art battery without changing the cell and system structure.<sup>14,15</sup> Various stress factors, including temperature,<sup>16–18</sup> current rates,<sup>19–21</sup> lower/upper cutoff voltage,<sup>22,23</sup> state of charge (SoC),<sup>24</sup> and cycling depth of discharge (DoD),<sup>25</sup> are considered in battery lifespan management to evaluate the battery durability and develop suitable usage strategies. Generally, high-temperature cycling accelerates the battery degradation reactions, such as active material loss and solid electrolyte interphase (SEI) film growth, leading to capacity fade.<sup>26,27</sup> High current rates produce higher diffusion stress, trigger cracks in the electrode particles, and enhance the battery degradation at moderate temperatures.<sup>28,29</sup> Appropriate control of temperature and current rates are usually the primary considerations in battery management for optimizing the battery operation strategy.<sup>30,31</sup> In addition, the cycling voltage range, i.e., a combination of cutoff voltage, SoC, and DoD, is also an important factor in the consideration of battery cycling tests. Gao et al.<sup>25</sup> investigated the aging mechanism of batteries with Li(Ni, Mn, Co)O<sub>2</sub> cathode cycled in five partitioned SoC ranges with 20% DoD, indicating that the dominant factor causing degradation was the loss of lithium inventory (LLI). Zhu et al.<sup>24</sup> proposed that a battery comprising LiNi<sub>0.5</sub>Co<sub>0.2</sub>Mn<sub>0.3</sub>O<sub>2</sub> (NCM) and LiNi<sub>0.9</sub>Co<sub>0.05</sub>Al<sub>0.05</sub>O<sub>2</sub> (NCA) as cathode blend and graphite as anode cycling in a medium SoC range results in lower capacity loss and behaves better than including high or low SoC in the cycling ranges and could minimize the risk of unexpected nonlinear capacity fade. Aiken et al.<sup>22</sup> designed a low-voltage operation method demanding the highest lifetime for pouch cells with LiNi<sub>0.5</sub>Mn<sub>0.3</sub>Co<sub>0.2</sub>O<sub>2</sub> cathode, showing that the pouch cells operated up to 3.65 and 3.80 V (approximately 0%–30% SoC and 0%–60% SoC, respectively) show superior capacity retention to that for the operation to 4.2 V (0%–100% SoC). No damage to the positive electrode is found, and the negative electrode passivation is identified as the most likely cause of capacity fade for the low-voltage operation. The aforementioned studies show that avoiding extreme voltages facilitates the development of battery lifetime by reducing the decay of the cathode material at high voltages.<sup>25,32,33</sup> The lifetime of a commercial 18650 cell is significantly prolonged by changing the cycling voltage window from 2.65–4.2 V (0%–100% SoC) to 3.1–4.2 V (10%–100% SoC) by avoiding the electrochemical activation of the Li<sub>0.75</sub>Si phase in the anode. However, a narrow design of the voltage window at the beginning of life (BoL) allows only partial usage of the whole energy capability, reducing the cell utilization efficiency, which goes against the design criteria of high energy density for long driving range in electrically operated devices (e.g., electric vehicle applications). Reports on taking into account battery utilization and long lifetime are few. Bharathraj et al.<sup>34</sup> simulated a dynamic charging protocol to prolong the battery cycle life, wherein the charge cutoff voltage was incremented in stages (up to the manufacturer-recommended maximum charge voltage) to have a trade-off between the increase in extractable per-cycle capacity and degradation that leads to capacity fade due to higher voltage cutoff values.

The purpose of this study is to prolong the battery service time while minimally compromising the extractable capacity during the whole life cycle. Batteries based on transition metal oxides (Li(TM)O<sub>2</sub>, TM = transition metal) as a cathode are cycled under different working conditions, exhibiting nonlinear and inconsistent degradation patterns as explained by the degradation on the anode side. A method of



raising the lower cutoff voltage before the cells enter the fast capacity fade region is proposed, which not only prolongs the battery cycle life but also improves the cell cycling consistency. The proposed method is verified on a total of three types of commercial lithium-ion batteries, which all provide longer service time in the whole life cycle and probably create stable profits in suitable second-use applications.

## RESULTS AND DISCUSSION

### Capacity fade and impedance change

The variations of capacity with the cycles as well as fitting parameters for impedance for type A cells are illustrated in Figure 1. The horizontal coordinates of Figures 1A–1D, 1G–1I are Ah throughput, which indicates the total charge of the battery during cycling since the cycle number for cells cycled in different voltage windows cannot directly be compared. The capacity fade results in Figure 1A show that the capacity of A1\_#1–A1\_#6 cells declines linearly until 1,500 Ah total throughput, and after that the capacity of A1\_#1 and A1\_#2 cells continues to decline linearly, whereas the

A1\_#3–A1\_#6 cells show a nonlinear degradation with an increasing rate among cells. It can be seen that the A1\_#1–A1\_#6 cells have different residual capacities when they reach the same throughput of 3,500 Ah (dotted line) expressing an inconsistent degradation in [Figure 1A](#). The A1\_#1 and A1\_#2 cells possess an excellent residual capacity of 73% and 75%, respectively, while the A1\_#3–A1\_#6 cells exhibit a residual capacity of 52%, 60%, 36%, and 69%, respectively. The groups A2 and A3 show similar capacity fade patterns as shown in [Figures 1B](#) and [1C](#). The A2\_#1–A2\_#3 cells show a linear capacity loss before 1,500 Ah throughput, then the A2\_#1 cell continues to show a linear capacity fade, meanwhile the A2\_#2 and A2\_#3 cells encounter a faster and nonlinear capacity fade. The A2\_#1–A2\_#3 cells have 73%, 66%, and 26% residual capacity, respectively, when achieving 3,500 Ah throughput as shown by the dotted line. The A3 cells show a similar capacity loss as the A1 and A2 cells. The A3\_#1, A3\_#2, and A3\_#4 cells have a linear capacity fade upon reaching the 3,500 Ah throughput as shown by the dotted line in [Figure 1C](#). In particular, the A3\_#3 cell shows a strong nonlinear capacity loss with zero residual capacity near 3,000 Ah throughput. The groups A1, A2, and A3 in [Figures 1A–1C](#) are cycled in the same voltage window of 2.5–4.2 V using different charge/discharge rates. It is noted that each group has a certain degradation threshold where the capacity of all cells declines linearly before the  $N^{\text{th}}$  cycle and in some cells nonlinearly afterward. The threshold occurs at a throughput of 1,400–1,800 Ah (300–400 cycles) corresponding to approximately 85% of the initial capacity for type A cells. The  $N^{\text{th}}$  cycle ( $N = 400$ ) is set in the cycle protocol of the A4, A5, and A6 groups. The lower cutoff voltage is raised to 3.3 and 3.0 V respectively after the  $N^{\text{th}}$  cycle in A4 and A5 with the same charge/discharge rate as A1. The charge/discharge rate is set to 0.5C/0.5C without changing the nominal voltage window for group A6. The capacity of cells in both groups A4 and A5 in [Figure 1D](#) shows a linear decrease as found either before or after the  $N^{\text{th}}$  cycle. All cells have an excellent residual capacity of around 70% at 3,500 Ah throughput. The average residual capacity of A4 and A5 is 71%, which is a 22% improvement compared with 49% for A1\_#3–A1\_#5, which also show poor consistency at the same cycling rate. The embedded figures of [Figures 1A](#) and [1D](#) depict the throughput of the A1, A4, and A5 battery groups when their residual capacity is at 70%. The A4\_#1–3 and A5\_#1–3 cells demonstrate an increase in average throughput by 38.1% and 22.5%, respectively, compared with the A1\_#3–6 cells. The capacity results of A6 are summarized in [Figure S2](#). It is seen that all cells show an accelerated capacity fade, only 50% capacity is obtained at 3,500 Ah throughput. By comparing the results in [Figures 1A–1D](#) and [S2](#), it can be deduced that increasing the lower cutoff voltage before the fast degradation threshold prolongs the battery life without changing the available capacity of the battery before the  $N^{\text{th}}$  cycle, and the inconsistent degradation of cells cycled under the same operating conditions is significantly improved in the course of cycling.

The impedance of representative cells from each group is extracted for the degradation analysis. The battery impedance changes during cycling as shown in [Figure 1E](#). The impedance curves gradually shift to higher values and two semi-circles enlarge with the battery degradation. An equivalent circuit model (ECM) in [Figure 1F](#) is used for the fitting of the experimental impedance spectra.  $R_0$  is the battery ohmic resistance.  $R_1//CPE1$  in parallel means the migration of lithium ions through the SEI in the high-frequency range. CPE is the constant phase element. Charge-transfer resistance ( $R_2$ ) in parallel with a CPE2 is used to model the charge-transfer process in the medium-frequency range.  $W$  is the Warburg impedance corresponding to semi-infinite diffusion in the low-frequency range. The fitted  $R_0$ ,  $R_1$ , and  $R_2$  of the representative cells are presented in [Figures 1G–1I](#) with all fitting coefficients of

determination ( $R2$ )  $>0.999$ . It is found that  $R0$  increases linearly for all representative cells until 1,400–1,800 Ah (approximately 300–400 cycles), then an accelerated increase in  $R0$  is observed for A1\_#3, A2\_#3, and A3\_#3 cells; meanwhile, the  $R0$  of A1\_#1, A4\_#1, and A5\_#1 cells continue to linearly increase. The resistance increment rate (the resistance increment from the initial value  $(R - R_{\text{initial}})/R_{\text{initial}}$ ) is calculated and marked in each figure for a quantitative discussion. At 3,000 Ah throughput of all cells, the  $R0$  of the A1\_#1, A4\_#1, and A5\_#1 cells has a rate of increment of 0.25, 0.24, and 0.22, respectively, whereas the increment rate of  $R0$  for the A1\_#3, A2\_#3, and A3\_#3 cells is 1.10, 0.49, and 0.40, respectively, which is about two to five times higher than that of the A1\_#1, A4\_#1, and A5\_#1 cells. The changes of  $R1$  in Figure 1H show a similar trend to that of  $R0$ . In particular, when the throughput of all cells is 3,000 Ah, the increment rate of  $R1$  for A1\_#1, A4\_#1, and A5\_#1 cells is 0.04, 0.49, and 0.30, respectively, meaning a minimal decay for these cells. Compared with that, the increment rate of  $R1$  for A1\_#3, A2\_#3, and A3\_#3 cells is 12.4, 2.32, and 2.2, respectively. A dramatic increase of  $R2$  is observed in Figure 1I, in which the rate of increment  $R2$  for the A1\_#3, A2\_#3, and A3\_#3 cells is 48.8, 92.8, and 280 respectively, while the increment rate of  $R2$  for A1\_#1, A4\_#1, and A5\_#1 cells shows 29.8, 21.1, and 29.3, respectively. By the comparison of Figures 1G–1I, the increment rate of  $R0$  is minimal, followed by  $R1$ , while the change of  $R2$  is much greater than  $R0$  and  $R1$ . The degradation threshold of impedance is observed to be in the range of 1,400–1,800 Ah (approximately 300–400 cycles), which is consistent with the capacity fade results.

### Degradation mechanism analysis

As stated in relation to the experiments, BoL, A1\_#3, and A4\_#1 cells are disassembled, and half-cells are made to investigate the change in the electrodes. The galvanostatic test results of the cathode half-cells are compared in Figure 2A. The cathode half-cells are charged and discharged at different current rates for a total of 18 cycles. The residual discharge capacity of the BoL cell is the largest, then A4\_#1 cell, and finally A1\_#3 cell except for a difference at 2C, where the residual discharge capacity of A4\_#1 and A1\_#3 cells is almost 0 and the residual discharge capacity of the BoL cell is still 60% of its nominal capacity. There is a large difference in the residual discharge capacity between C/3 and 2C, indicating severe polarization in the cathode. The alternating current (AC) impedance curves are compared in Figure 2B. The impedance of the cathode half-cells increases drastically after cycling, as seen from the comparison. An obvious shift of the A4\_#1 and A1\_#3 cells is seen in the embedded figure in Figure 2B, meaning the increase of ohmic resistance (the intercept with the real axis at high frequencies); meanwhile, the impedance arc in the medium-frequency range enlarges simultaneously, which is understood as an increase of the electrochemical polarization.

The *in situ* X-ray diffraction (XRD) patterns at selected  $2\theta$  ranges for the fresh and fatigued cathode are plotted in Figure 2C. No appearance of new reflections means the absence of new crystalline phase formation and structural damage. A series of phase transitions (i.e., H1  $\rightarrow$  M  $\rightarrow$  H2  $\rightarrow$  H3) is proved to occur during the charging and process of Ni-rich layered cathode materials.<sup>35</sup> The (003)NCA reflection and (104)NCA reflection of the BoL cell are observed at high voltage, but the reflections of NCA and NCM materials are difficult to separate in the A4\_#1 and A1\_#3 cells. Thus, only one rhombohedral structure ( $R-3m$ ) model is used for the *in situ* XRD patterns in Figure 2C with the Rietveld method in FullProf.<sup>36</sup> The averaged crystal structure parameters are presented in Figure S3. The difference between charging and discharging increases in both  $a$  and  $c$  in the fatigued cells, which means an increase of overpotential in the electrode. The variations of  $a$  and  $c$  for A4\_#1 and A1\_#3 cells

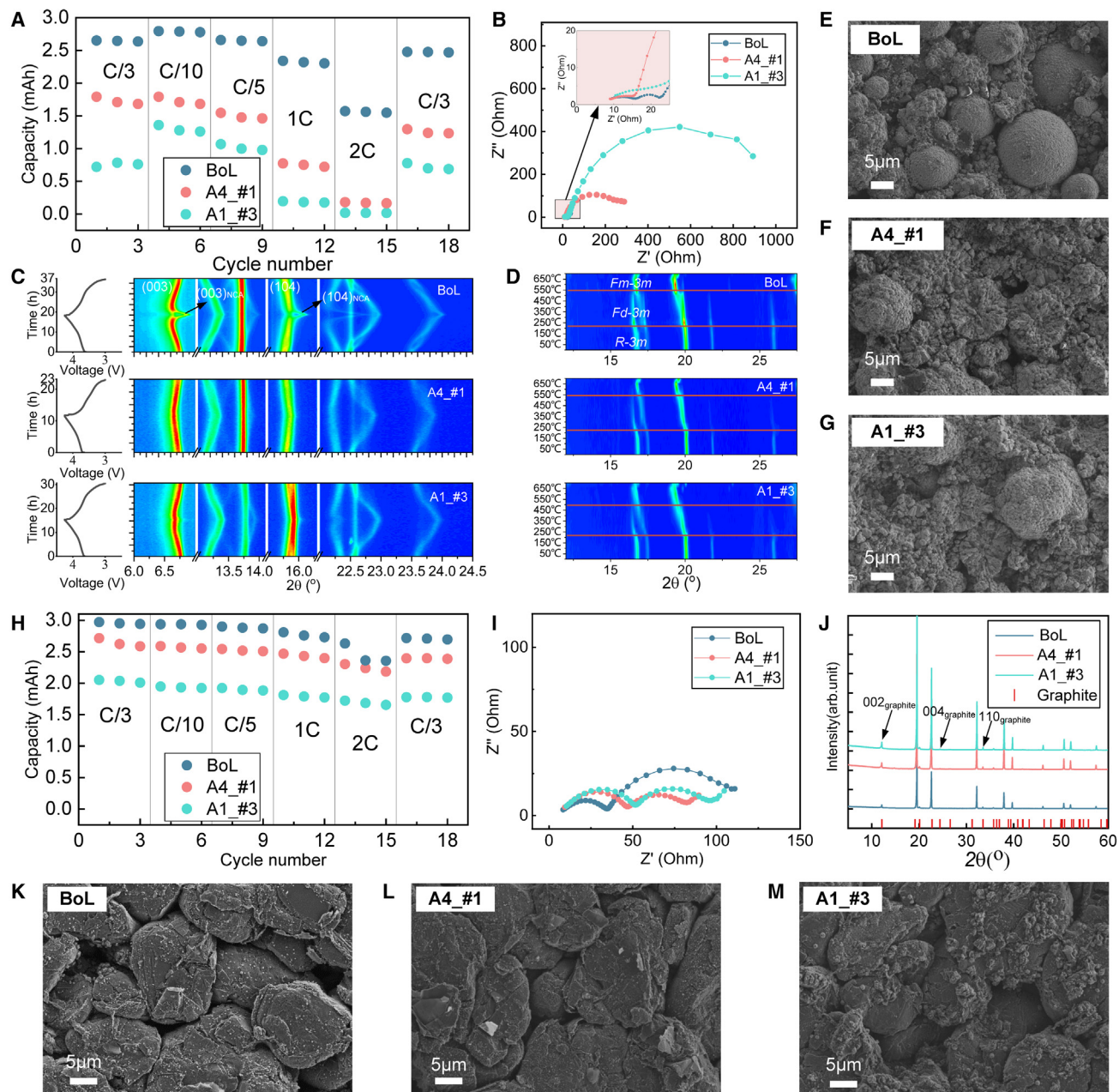


**Figure 2. Analysis of battery degradation mechanisms**

(A and B) Summary of discharge capacity (A) and AC impedance curve of the cathode half-cells (B).

(C and D) The *in situ* XRD patterns of cathode half-cells (C) and *in situ* TR-XRD patterns of the cathode (D).

(E–G) The SEM images of the cathode facing the current collector for the BoL cell (E), A4\_#1 (F), and A1\_#3 (G). The scale bar is 5  $\mu\text{m}$ .

(H and I) Summary of discharge capacity (H) and AC impedance curve of the anode half-cells (I).

(J) The *ex situ* XRD patterns of the anode.

(K–M) The SEM images of the anode facing the current collector for the BoL cell (K), A4\_#1 (L), and A1\_#3 (M). The scale bar is 5  $\mu\text{m}$ .

become narrow, supporting more incomplete de-lithiation of lithium in the cathode after cycling, as some lithium is trapped in the cathode, leading to the lithiated cathode loss,<sup>37</sup> which agrees with the capacity test results in Figure 2A. It can be concluded that no new diffraction peaks from unidentified phases are observed in the cycled cells, which indicates that the electrodes do not decompose into other

crystalline phases. The *in situ* temperature-resolved XRD (TR-XRD) test provides the average structural changes through phase transitions during thermal decomposition, which is useful to compare the thermal stability behavior of cathode materials. For the BoL cell, an *R-3m* wherein the phase transition from this phase to the disordered spinel (*Fd-3m*) phase starts at about 225°C (marked in Figure 2D), and the phase transition from spinel to rock-salt phase starts at about 550°C. The phase transition temperatures of the A4\_#1 cell are similar to those of the BoL cell. The phase transition from spinel to rock-salt phase occurs around 500°C for the A1\_#3 cell. During the heating, the transition metal cations migrate into the lithium layers where vacancies had been created during the full lithiated process. The random mixing of cations in each layer leads the layered rhombohedral structure to change into the spinel structure, and finally to the rock-salt structure.<sup>38,39</sup> An oxygen release is also observed during the structural transition from the initial layered structure to the NiO-type rock-salt structure in Nam et al.<sup>39</sup> It is suspected that the decrease of the phase transition temperature of A1\_#3 cell affords the information of a more likely mixing of cations and oxygen release, indicating a decrease in the thermal stability of the cathode after the full voltage window (2.5–4.2 V) cycling. The capacity and impedance results suggest that both thermodynamic and kinetic losses occur in the cathode of A4\_#1 and A1\_#3 cells, but A4\_#1 cell behaves better than A1\_#3 cell, which is consistent with the *in situ* XRD and TR-XRD. The scanning electron microscopy (SEM) images of the cathode facing the current collector are presented in Figures 2E–2G, in which the cathode particles are obviously cracked in the A4\_#1 and A1\_#3 cells. The SEM images of one cell in group A1 at 400 cycles are appended in Figure S4A, showing similar morphology with Figures 2F and 2G. The microcracks can be explained by the working current causing an increase in internal stress. High anisotropic strain generated upon repeated lithium insertion and extraction of the host lattice promotes the growth of microcracks that eventually cause the disintegration of the polycrystalline secondary particles, resulting in transport hindrance for ions and electrons. The SEM images of the cathode facing the separator are supplemented in Figures S4B–S4E. No obvious changes can be found as the surfaces of the cathode facing the separator are pressed by a rolling process in battery manufacturing, but many dissociated particles appear on the surface of the A1\_#3 cathode. The dissociated particles are verified as the disintegration of NCM and NCA by the energy-dispersive X-ray spectroscopy (EDX) results in Figure S4F, which is deemed to contribute to the decrease of the thermal stability of A1\_#3 cell.

The galvanostatic test results for the anode half-cells in a voltage window of 2–0.01 V are shown in Figure 2H. Compared with the cathode, the anode in the fatigued cells shows better energy and power performance. The output capacity sorted from large to small is BoL cell, A4\_#1 cell, and A1\_#3 cell. The electrochemical polarization of the anode is insignificant, as shown by the narrow difference in the residual discharge capacity between C/3 and 2C. The impedance of the anode half-cells in Figure 2I shows an enlargement in the high-frequency range, otherwise a shrinkage in the medium-frequency range, which means that the SEI resistance increases and the charge-transfer resistance decreases in the cycled anode. A possible explanation for the shrinkage of the impedance in the medium-frequency range is that the layered graphite surface area increases because of the fragmentation of material. This may accelerate the (de-)intercalation reaction more than the hampering from the SEI growth.<sup>40–42</sup> The change in the impedance indicates less polarization between the BoL and the cycled cells. The *ex situ* XRD patterns show that no additional bulk phases appear beside the graphite in Figure 2J. The typical flake structure of graphite can be seen for all cells, as presented in Figures 2K–2M and S5, and dense depositions and aggregation are observed on the surface of the fatigued A1\_#3

anode both facing the current collector and separator as shown in Figures 2M and S5E, respectively. A similar anode morphology including unusual spherical particles is observed in Surace et al.<sup>43</sup> in which the unusual spherical particle is verified as the decomposition of the fluoroethylene carbonate (FEC)-containing electrolyte upon cycling. The high concentration of fluorine species in the  $\text{LiPF}_6$  electrolyte increases the probability of creating many fluorine-containing nucleation centers, where the chemical species nucleate and grow from both FEC and  $\text{LiPF}_6$  decomposition according to crystal nucleation theory.<sup>44</sup> The electrolyte of type A battery is extracted by a centrifugal machine, and tested by gas chromatography-mass spectrometry (GC-MS), proving that the ratio of FEC to ethylene carbonate (EC) is 4 wt % to 47 wt % (FEC/EC 4/47 wt %) in the electrolyte (see Figure S6). The consumption of the electrolyte reduces the recyclable lithium and causes an increase in the SEI resistance,<sup>45</sup> resulting in the continuous growth of the surface layer, and more formation of the surface layer reduces the material porosity and hinders lithium movement into the anode, leading to the loss of battery capacity. In summary, the cathode from A4\_#1 and A1\_#3 cells shows both kinetic and thermodynamic loss, which is related to the microcracks and disintegration of the cathode secondary particles. The anode shows mainly thermodynamic loss as the electrochemical polarization is not obvious. Dense deposition and aggregation structures are observed from the SEM images, which is proposed to be a result of the decomposition of the electrolyte and the interface reaction leading to a faster capacity loss.

### Discussion of the degradation inconsistency

The aforementioned discussion indicates that the nonlinear capacity fade is related to the deposition on the anode surface, which is most likely from the decomposition of the FEC in the electrolyte, meaning that the degradation inconsistency between different cells is relevant for the decomposition of FEC and the degree of decomposition. Studies indicate that a high potential of anode vs.  $\text{Li}^+/\text{Li}$  in the full cell (cathode vs. anode) triggers the decomposition of FEC.<sup>43</sup> Therefore, the potential of the anode vs.  $\text{Li}^+/\text{Li}$  during cycling is investigated. The cathode vs.  $\text{Li}^+/\text{Li}$ , anode vs.  $\text{Li}^+/\text{Li}$ , and full cell curves from the three-electrode cell in which the solid line and dotted line indicate the discharge rate of 0.824 and 0.1 mA are illustrated in Figure 3A, respectively. The differential voltage (DV) curve corresponding to Figure 3A for the 0.1-mA discharge is presented in Figure 3B. There are four peaks in the DV curve of the full cell in which CA1 and CA2 peaks are from the cathode, and AN1, AN2, and AN3 peaks are from the anode, while CA1 and AN1 peaks are overlapping. Usually, the DV curves are used for degradation mechanism analysis according to the changes in peak positions.<sup>37,46,47</sup> During cycling, the shortening of L1 represents the loss of cathode active material, and the shortening of L2 represents the loss of anode active material. The L3 represents the relative voltage windows of the cathode vs.  $\text{Li}^+/\text{Li}$  and anode vs.  $\text{Li}^+/\text{Li}$  curves, whose variation is related to the LLI. The relative positions of the cathode and anode are determined by the DV analysis. Figure 3C shows the discharge curves of one type A cell in group A1. The gradient line represents the high-rate (1C) discharge curve in each cycle, and the separated blue line represents the low-rate (C/25) discharge curve in every 100 cycles. The relaxation voltage at the end of the high-rate discharge is marked in Figure 3C, which shows an increasing trend as the cycle increases. The DV analysis is conducted on the C/25 discharge curve as obvious peaks can be derived due to the low polarization. A method using the relaxation voltage probing the potential of anode vs.  $\text{Li}^+/\text{Li}$  is proposed by bridging the discharge voltage curve at C/25 and C/3, as illustrated in Figures 3A and 3D.

The voltage corresponding to the 0.1-mA discharge curve (solid line referring to the time[seconds], x axis) in Figure 3A is treated as a pseudo-open circuit voltage (OCV).

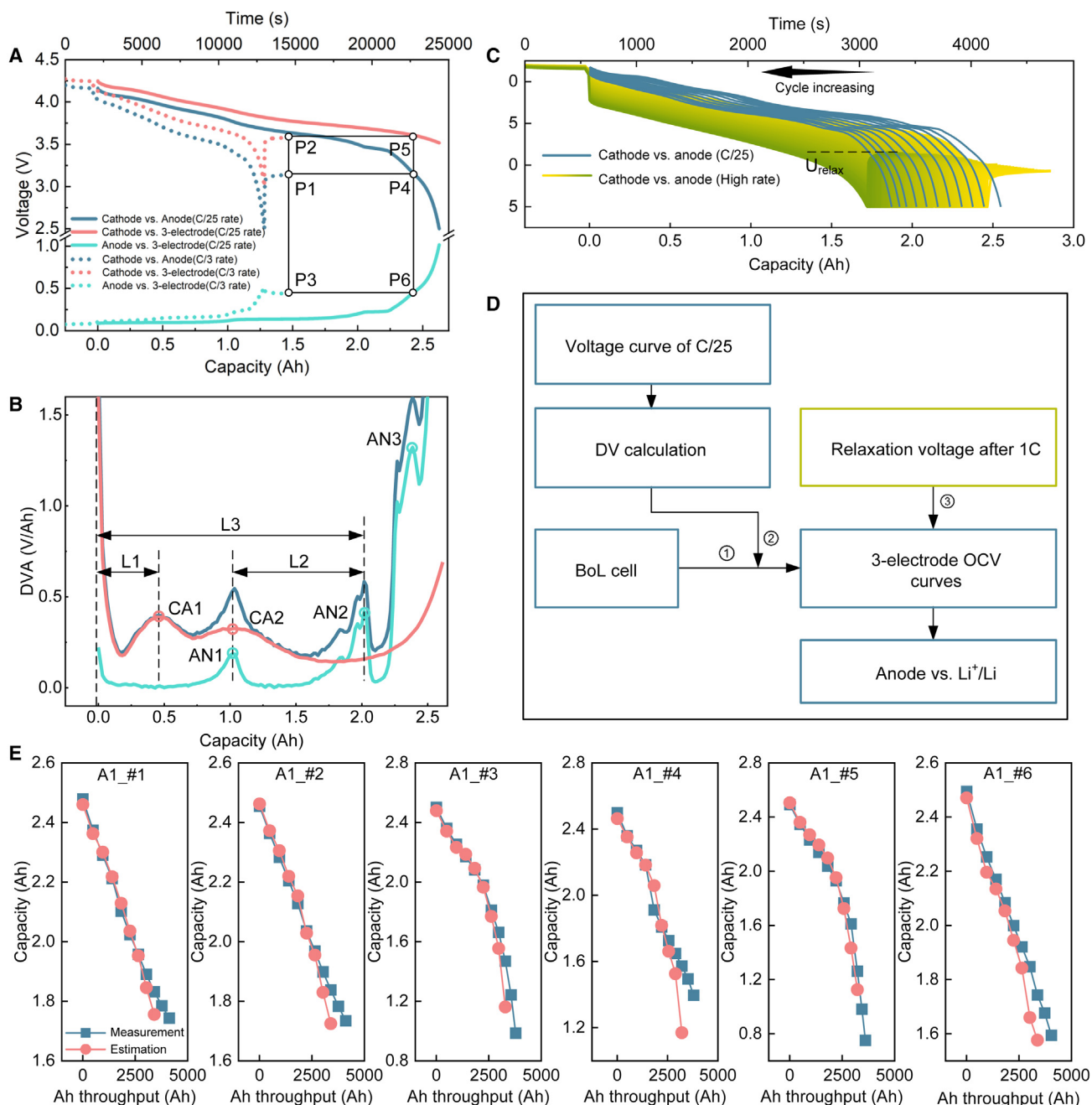


**Figure 3. Results of the cell degradation inconsistency**

- (A) Voltage curves from the three-electrode cell.  
 (B) A schematic plot of the DV curve.  
 (C) Voltage change during cycling.  
 (D) Voltage identification strategy.  
 (E) Comparison of the battery capacity from the measured and estimated.

The relaxation voltage of the 0.824-mA discharge curve (dashed line referring to the capacity [Ah], x axis) for the full cell is named point 1 (P1), and the corresponding voltages of cathode vs.  $Li^+/Li$  and anode vs.  $Li^+/Li$  are defined as P2 and P3, respectively. When the P1 is obtained experimentally, the same voltage point P4 can be determined from the 0.1-mA discharge curve, as shown in Figure 3A. Then, the

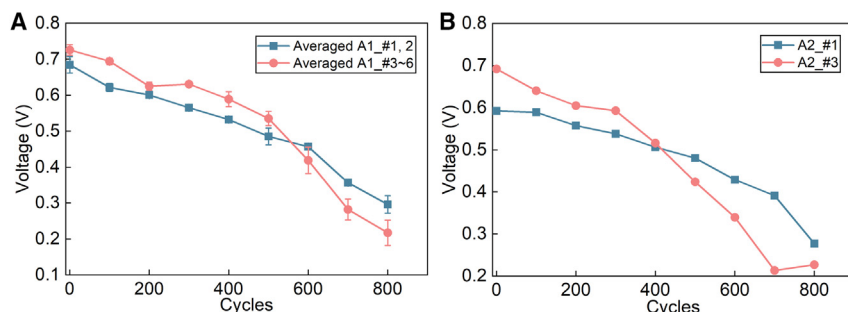


**Figure 4. Cycling performance**

(A) The identified cutoff voltage of anode vs.  $\text{Li}^+/\text{Li}$  for the A1 group. The voltage of the cells with good (A1\_#1–A1\_#2) and weak (A1\_#3–A1\_#6) performance is averaged, respectively. Data are represented as mean  $\pm$  SD.

(B) The identified cutoff voltage of anode vs.  $\text{Li}^+/\text{Li}$  for the A2 group.

voltage of cathode vs.  $\text{Li}^+/\text{Li}$  (P5) and anode vs.  $\text{Li}^+/\text{Li}$  (P6) corresponding to the P4 can be obtained by making the vertical line through P4 once their relative positions are determined on the 0.1-mA discharge curve. Meanwhile, it is found that the relaxation voltage of high-rate discharge (0.824 mA) for cathode vs.  $\text{Li}^+/\text{Li}$  (P2) and anode vs.  $\text{Li}^+/\text{Li}$  (P3) is equal to the voltage of P5 and P6, respectively, meaning that the relaxation voltage of high-rate discharge for cathode vs.  $\text{Li}^+/\text{Li}$  and anode vs.  $\text{Li}^+/\text{Li}$  is deduced from the voltage relaxation of high-rate discharge of the full cell based on the C/25 rate discharge curve for cathode vs. anode if the pseudo-OCV curves for cathode vs.  $\text{Li}^+/\text{Li}$  and anode vs.  $\text{Li}^+/\text{Li}$  are identified. Hence, a voltage identification flowchart is proposed in Figure 3D. First, the OCV curves of cathode vs.  $\text{Li}^+/\text{Li}$ , anode vs.  $\text{Li}^+/\text{Li}$ , and cathode vs. anode for the cell at the BoL state are obtained by the three-electrode test as the baseline (⊙). Second, the DV curve is processed by differentiating the voltage with respect to the capacity during cycling. The change and offset between the cathode and anode OCV curves for the cycled cell are deduced by identifying the change of the peak of the DV curve (see the section “voltage identification method” in “experimental procedures” ⊕). Finally, the potential of anode vs.  $\text{Li}^+/\text{Li}$  after relaxation for the cycled cell can be gained by combining the offset OCV curves and the relaxation voltage as demonstrated from P1 to P6 in Figure 3A (⊙). A capacity value is treated as an estimated capacity once P4 is determined. The real tested capacity from P1 and estimated capacity from P4 match well in Figure 3E, which verifies the reliability of the voltage identification method.

The cells are classified as good and bad cells based on whether they demonstrate a linear decline in capacity over time. The identified working potential of anode vs.  $\text{Li}^+/\text{Li}$  for cells with good performance (A1\_#1–A1\_#2) and cells with weak performance (A1\_#3–A1\_#6) are lower than 0.8 V, as shown in Figure 4A. There is no copper dissolution in the anode because it is verified that copper dissolution begins when the anode potential exceeds 3.56 V vs.  $\text{Li}^+/\text{Li}$  theoretically.<sup>48,49</sup> The anode vs.  $\text{Li}^+/\text{Li}$  for cells A2\_#1 (good performance) and cells A2\_#3 (weak performance) with 2C/2C charge and discharge rate are shown in Figure 4B. It is found that the anode vs.  $\text{Li}^+/\text{Li}$  is higher for the cells with weak cycling performance than that of the cells with excellent cycling performance in the early cycles (before 400–600 cycles), as shown in Figures 4A and 4B. From Figure S7, the cathode vs.  $\text{Li}^+/\text{Li}$  is located above 2.9–3.3 V at the end of discharge; in addition, the full cells are cycled to 4.2 V, indicating that no transition metal dissolution appears as the transition metal dissolution usually occurs at elevated charge cutoff voltages (beyond 4.4 V vs.  $\text{Li}^+/\text{Li}$ ).<sup>50,51</sup> The cathode working potential of cells with good performance is higher than that of the

weak-performance cell, meaning a narrower cycling voltage window facilitating the stability of the cathode material, which is consistent with the analysis in section “[degradation mechanism analysis](#).” The high potential of anode vs.  $\text{Li}^+/\text{Li}$  in the early cycles is speculated to be the reason triggering nonlinear and inconsistent battery degradation since it has been interpreted as the decomposition of the FEC caused by a high potential of the anode as observed on anode SEM images in [Figure 2M](#). It also explains the good performance of cell whose lower cutoff voltage increased from 2.5 V to 3 V/3.3 V in [Figure 1D](#), as the increase of full cell voltage leads to a decrease of the anode vs.  $\text{Li}^+/\text{Li}$  potential, which can be seen as one of the contributing factors in the suppression of rapid battery degradation. Detailed discussion is given in the next section. In addition, from [Figure 4](#), it can be observed that the identified cutoff voltage of anode vs.  $\text{Li}^+/\text{Li}$  starts to rapidly decrease when the battery experiences rapid capacity fade. Therefore, in practical applications, the first step is to utilize the proposed method to identify the cutoff voltage for anode vs.  $\text{Li}^+/\text{Li}$ , as shown in [Figure 3D](#). Subsequently, the rate of decay of the identified cutoff voltage of anode vs.  $\text{Li}^+/\text{Li}$  is used to determine the starting of raising the lower cutoff voltage.

#### Verification of the lifetime prolonging method

By the observation of P1, P2, and P3 in [Figure 3A](#), the polarization of the anode is lower than that of the cathode due to its higher electrical conductivity and low polarization during delithiation. It is assumed that, when approaching the cutoff voltage, the accelerated voltage drop is ascribed to the polarization of the cathode and the potential increase of the anode. The polarization from the cathode side cannot be regulated by operating conditions, but the anode can be shifted toward a lower working potential by increasing the battery cutoff voltage. From the results in [Figures 4A](#) and [4B](#), the anode potential decreases from 0.7 V to 0.2 V in the course of cycling, and it is around 0.5 V at approximately 400 cycles. A strategy to increase the cutoff voltage from 2.5 V to 3 V and 3.3 V respectively is proposed before the cell enters the fast degradation region (after 85% of the initial capacity for type A cells), as shown in [Figure 5A](#). The changes of the cycling voltage window lead to approximately 10% and 20% SoC loss compared with the full voltage window (2.5–4.2 V) at the 400<sup>th</sup> cycle. The relaxation voltage goes back to 3.35 and 3.5 V, as shown in [Figure 5B](#), and the corresponding anode potential goes from 0.60 V down to 0.32 V for A5\_#1 cell, and from 0.63 to 0.23 V for A4\_#1 cell, as shown in [Figure 5C](#) by the method in [Figure 3D](#). In total, the cathodes do not show obvious change and always operate within an appropriate voltage range, which is responsible for the working stability. The increase of the cutoff voltage keeps the anode working in a low potential range after 400 cycles and outside the FEC decomposition region, which corresponds to the good cycling performance in [Figure 1D](#), and the degradation mechanisms are verified in [Figure 3](#).

Two other cell types (type B and type C) are used to verify the proposed lifetime prolonging method. The capacity change of type B is illustrated in [Figure 5D](#), and B1 and B2 mean different cycling protocols, as illustrated in [Table 1](#). The cells without any change (B1) show an accelerated capacity decay after 150 cycles (approximately 90% of the initial capacity). The lower cutoff voltage is raised from 2.65 to 3.0 V after 150 cycles for the B2 cells, and it can be found that a 16.7% Ah throughput increase is obtained at 70% of its BoL capacity, and 24.5% Ah throughput is achieved at 50% (BoL capacity is the average of initial capacities for each type cell). The corresponding impedance is shown in [Figure 5E](#). The impedance is similar for B1\_#1 and B2\_#1 at the BoL state, and the resistances increase with battery cycling. When the Ah throughput approaches 1,240 Ah, all the resistances of B2\_#1 are less than that of the B1\_#1 cell in [Figure 5F](#). The cycling results of type C are similar to type B. The

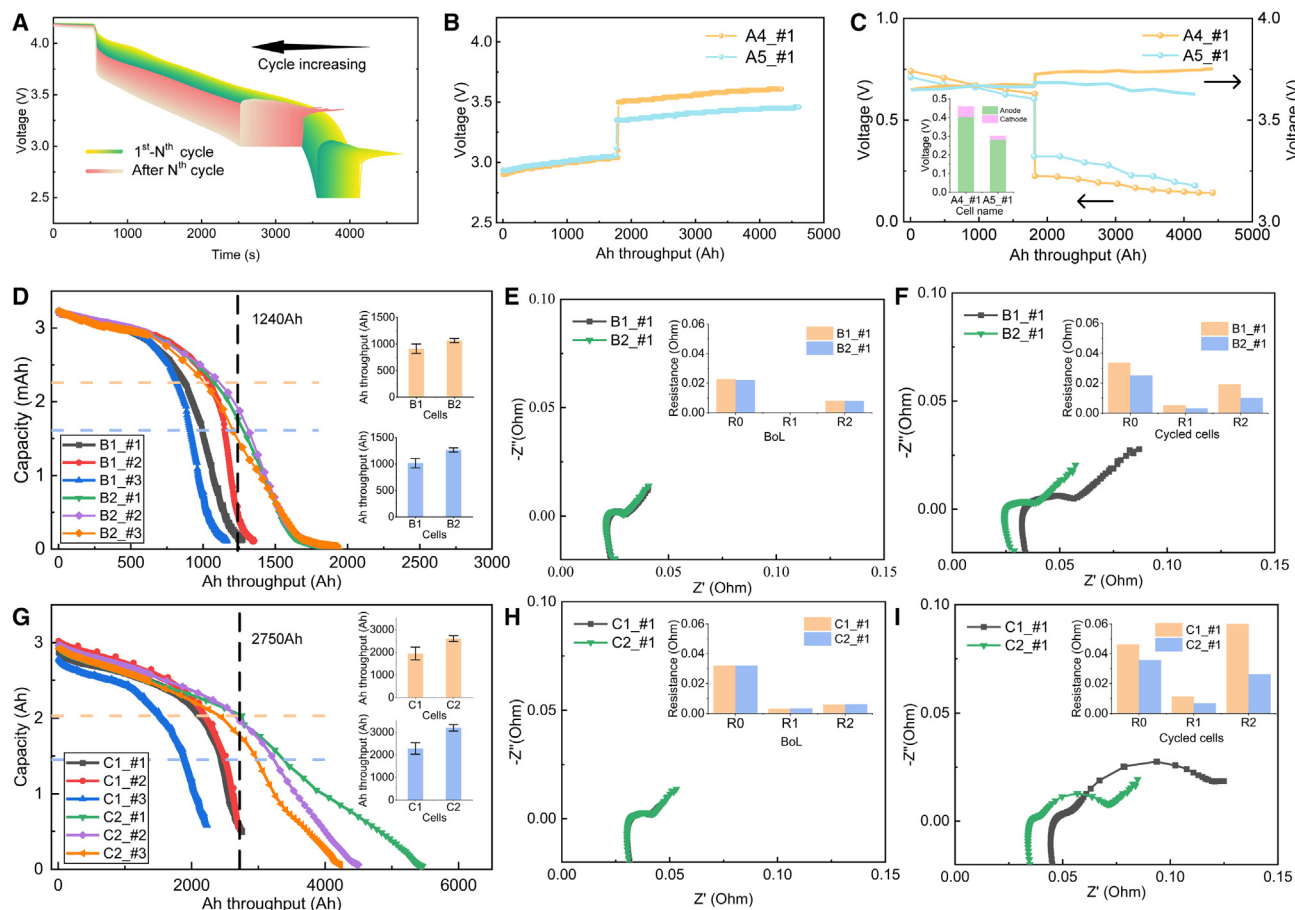


**Figure 5. Verification of the lifetime-prolonging method**

(A) Voltage curves of the A4\_#1 cell during cycling, including first  $N^{\text{th}}$  and after  $N^{\text{th}}$  cycle ( $N = 400$ ).

(B) The relaxation voltage of the A4\_#1 and A5\_#1 cells after full discharge.

(C) The calculated potential of cathode vs.  $\text{Li}^+/\text{Li}$  and anode vs.  $\text{Li}^+/\text{Li}$ , in which the contribution of cathode and anode for the abrupt full cell potential change are compared in the embedded figure.

(D) The capacity change of type B.

(E and F) The AC impedance result for the type B at the BoL state (E) and the result for the type B (F) at the fatigued state.

(G) The capacity change of type C.

(H and I) The AC impedance result for the type C at the BoL state (H) and the result for the type C (I) at the fatigued state. The embedded plots in (D) and (G) are the average Ah throughput at 70% and 50% of the BoL capacity. Data are represented as mean  $\pm$  SD. The embedded figures in (E), (F), (H), and (I) show the calculated R0, R1, and R2.

capacity threshold occurs around 200 cycles (approximately 85% of the initial capacity). A 33.7% and 40.3% capacity extension is achieved at 70% and 50%, respectively, after the increase of the lower cutoff voltage from 2.5 to 3.0 V, as shown in Figure 5G. The cells (C1\_#1, and C2\_#1) show very close resistances at the beginning in Figure 5H, but an obvious difference occurs for each resistance when it reaches 2,750 Ah in Figure 5I. From the test results of type B and type C cells, it is verified that the proposed battery life prolongation method is effective and beneficial to the reduction of battery thermodynamic and kinetic loss.

Comparing the lifetime prolonging results of type A, B, and C batteries reveals that, under the same operating strategies, i.e., raising the lower cutoff voltage to 3 V after  $N$  cycles (Table 1), the throughput of type A, B, and C cells increased by 38.1%, 16.7%, and 33.7%, respectively, when the capacity degradation reached 70%.

**Table 1. Summary of the 18650-type battery tests**

| Cycling protocols | Cell numbers | Charge/discharge rate (C) |                       | Voltage window (V)    |                       | Check-up tests  |  |   |
|-------------------|--------------|---------------------------|-----------------------|-----------------------|-----------------------|---|--|---|
|                   |              | First-N <sup>th</sup>     | After N <sup>th</sup> | First-N <sup>th</sup> | After N <sup>th</sup> | Residual capacity   | AC impedance   | DV  |
| A1                | 6            | 1/1                       | 1/1                   | 2.5–4.2               | 2.5–4.2               | charge:<br>0.5C, 4.2 V, C/25<br>discharge:<br>1C, 2.5 V<br>every 100 cycles | 10 kHz–0.01 Hz, 250 mA<br>100%, 0% SoC<br>every 100 cycles | charge:<br>C/25, 4.2 V<br>discharge:<br>C/25, 2.5 V<br>every 100 cycles |
| A2                | 3            | 2/2                       | 2/2                   | 2.5–4.2               | 2.5–4.2               |   |  |   |
| A3                | 4            | 1/1                       | 2/2                   | 2.5–4.2               | 2.5–4.2               |   |  |   |
| A4                | 3            | 1/1                       | 1/1                   | 2.5–4.2               | 3.3–4.2               |   |  |   |
| A5                | 3            | 1/1                       | 1/1                   | 2.5–4.2               | 3.0–4.2               |   |  |   |
| A6                | 3            | 1/1                       | 0.5/0.5               | 2.5–4.2               | 2.5–4.2               |   |  |   |
| B1                | 3            | 0.5/1                     | 0.5/1                 | 2.65–4.2              | 2.65–4.2              | charge:<br>0.5C, 4.2 V, C/20<br>discharge:<br>1C, 2.65 V<br>every 25 cycles | 10 kHz–0.01 Hz<br>20 mV<br>100%, 0% SoC<br>every 25 cycles | charge:<br>C/25, 4.2 V<br>discharge:<br>C/25, 2.65 V<br>every 25 cycle  |
| B2                | 3            | 0.5/1                     | 0.5/1                 | 2.65–4.2              | 3.0–4.2               |   |  |   |
| C1                | 3            | 0.5/1                     | 0.5/1                 | 2.5–4.2               | 2.5–4.2               | charge:<br>0.5C, 4.2V, C/20<br>discharge:<br>1C, 2.5V<br>every 50 cycles    | 10 kHz –0.01 Hz, 20 mV<br>100%, 0% SoC<br>every 50 cycles  | charge:<br>C/25, 4.2 V<br>discharge:<br>C/25, 2.65 V<br>every 50 cycles |
| C2                | 3            | 0.5/1                     | 0.5/1                 | 2.5–4.2               | 3.0–4.2               |   |  |   |

N is set as 400 for type A, 150 for type B, and 200 for type C according to their degradation patterns.

This indicates that there are differences in the effectiveness of the three types of batteries in lifetime prolonging. One potential factor contributing to the differential effectiveness of lifetime prolonging may lie in the existence of battery specificity; e.g., given the distinct cathode electrode materials of type A, B, and C cells, the optimal adjustment of lower cutoff voltage may vary.

This study proposes a method for prolonging the battery cycle life and enhancing the battery consistency in the full life cycle. The cycling experiment of 18650 lithium-ion batteries indicates that nonlinear capacity degradation with a large dispersion occurs around approximately 85% of the initial capacity, which is taken as the degradation threshold. The battery degradation is proposed as a result of the decomposition of the electrolyte and the interface reaction verified by the result of electrochemical analysis and multiscale postmortem analysis. The inconsistent degradation is assumed to be triggered by the change of potential of the anode vs. Li<sup>+</sup>/Li. A method for prolonging the battery cycle lifetime is proposed, in which the lower cutoff voltage is raised to 3 V when the battery reaches a capacity degradation threshold where the nonlinear and inconsistent degradation occurs. It shows that the battery can have a 38.1% improvement in throughput compared with the cell of poor consistency performance at 70% of their BoL capacity, along with an improvement in consistency. The proposed method is verified on two other types of commercial lithium-ion batteries, the cycle lifetime extension of 16.7% and 33.7% is achieved at 70% of their BoL capacity, respectively, and it is 24.5% and 40.3% capacity extension at 50% of their BoL capacity, respectively. Results indicate that the battery life is extended and the consistency of the batteries is improved without the reduction of battery utilization in the early life. The research provides new insights into battery management to prolong the battery lifetime and improve the battery consistency at the full life cycle.

## EXPERIMENTAL PROCEDURES

### Resource availability

#### Lead contact

Further information and requests for resources should be directed to the lead contact, Jiangong Zhu ([zhujiangong@tongji.edu.cn](mailto:zhujiangong@tongji.edu.cn)).

### Materials availability

This study did not generate new unique materials.

### Data and code availability

The data used to generate the plots in this study are available in the supplemental information as [Data S1](#). Any other data in this study are available from the corresponding author upon reasonable request.

### Battery cycling

Long-term cycling is conducted on three types of commercial 18650 batteries, with a summary of cycling conditions provided in [Table 1](#). The cycling protocols are named AX, BX, and CX, respectively. A, B, and C correspond to different battery types. X represents different groups using the same battery type. The quantity of the cell samples is listed in the brackets following AX, BX, and CX, which ranges from 3 to 6 in each cycling protocol to ensure reproducibility of the test. The positive electrode of the type A battery is a blend of 42 (3) wt %  $\text{Li}(\text{Ni}_{0.5}\text{Co}_{0.2}\text{Mn}_{0.3})\text{O}_2$  to 58 (3) wt %  $\text{Li}(\text{Ni}_{0.9}\text{Co}_{0.05}\text{Al}_{0.05})\text{O}_2$ , and the negative electrode is graphite from Zhu et al.<sup>37</sup> The positive electrode compositions of the type B battery and type C battery are  $\text{Li}(\text{Ni}_{0.86}\text{Co}_{0.11}\text{Al}_{0.03})\text{O}_2$  and  $\text{Li}(\text{Ni}_{0.83}\text{Co}_{0.11}\text{Mn}_{0.07})\text{O}_2$  respectively, and the negative electrodes for both cell types have roughly 97 wt % C and 2 wt % Si as well as traces of H, N, and S from Sørensen et al.<sup>52</sup> Detailed specifications of the three types of batteries are provided in [Table S1](#). The charge/discharge rate and voltage window are the main factors in each cycling protocol. The charge/discharge rate is calculated from the nominal battery capacity; i.e., 1C is equal to 2.5 A for the type A cells, and 1C is equal to 3.5 A for type B and C cells. The “first- $N^{\text{th}}$ ” and “after  $N^{\text{th}}$ ” mean adjustment of charge/discharge rate or voltage window before and after the  $N^{\text{th}}$  cycle. Different N is used to adapt to the difference of the degradation patterns for the three battery types. Using A4 as an example, three cells are cycled with a constant charge/discharge rate of 1C, in a full voltage window (2.5–4.2 V) for the first to the 400<sup>th</sup> cycle (N is equal to 400 for type A cell), and the voltage window changes to 3.3–4.2 V after the 400<sup>th</sup> cycle. The check-up tests, including residual capacity, AC impedance, and DV, are set for all cycled cells. For type A cells, every 100 cycles, the cells are fully charged to 100% SoC with a charging protocol, which is a 0.5C charge up to 4.2 V followed by a constant voltage (CV) step until the current is below C/25, and then the residual capacity is tested using a 1C discharge to 2.5 V, each followed by an AC impedance test at full charge and full discharge in a range of 10 kHz to 0.01 Hz with a sinusoidal amplitude of 100 mA. A charge/discharge curve with C/25 is obtained for the DV analysis. Similar check-up tests are conducted on type B and type C cells but using different setting parameters, as shown in [Table 1](#). The cycling tests and check-up tests are performed using a Biologic BCS potentiostat. The cycling environment is controlled at 25°C in a climate chamber (BINDER,  $\pm 0.2^\circ\text{C}$ , Germany).

### Battery disassembling and electrochemical tests

One type A cell at the BoL and A4\_#1 and A1\_#3 cells after cycling are disassembled at a fully discharged state under argon atmosphere in a MBraun glove box. The battery disassembling procedure is referred to in the flow chart in a previous study.<sup>53</sup> Cathode half-cells and anode half-cells of CR2032 type are assembled for independent electrochemical characterization for BoL, A4\_#1, and A1\_#3. The electrode materials are taken halfway from the unfolded jelly-roll electrode sheet. Since the electrodes are double coated in the commercial batteries, one side of the electrode coating is removed using N-methyl-2-pyrrolidone (NMP) and the residual electrode is washed in dimethyl carbonate (DMC) and punched out in discs with a 12-mm

diameter. The half-cells have the anode or cathode as the working electrode and metallic lithium as a counter electrode. A Celgard separator is used for the half-cells. lithium hexafluorophosphate ( $\text{LiPF}_6$ ) (1 M) in a mixture of DMC and EC at a volume ratio of 1:1 is used as the electrolyte. The cathode and anode half-cell experiments are conducted in potential ranges of 4.25–3 V and 2–0.01 V, respectively. Galvanostatic measurements ranging from C/10 to 2C (1C = 2.47 mA for half-cells) are used to obtain fundamental information about the battery, such as residual capacity, high-rate performance, and cycle stability. The AC impedance is tested in full-charge and full-discharge states in a range of 10 kHz to 0.01 Hz with a sinusoidal voltage signal of 5 mV for the half-cells. A Swagelok three-electrode cell using the cathode and anode from the BoL cell plus metallic lithium as a reference electrode is used to monitor the initial potential shift of the cathode vs.  $\text{Li}^+/\text{Li}$  and anode vs.  $\text{Li}^+/\text{Li}$ . The three-electrode cell measurements are performed with 0.824 mA and 0.1 mA at 25°C using the same cutoff voltage as for the commercial cells (i.e., between 2.5 and 4.2 V). The electrolyte of type A cells is collected by a centrifugal machine, and the composition is tested by a GC-MS (Agilent GC-MS 7980B 5977B).

### SEM-EDX and XRD techniques

The morphologies of the cathode and anode are obtained using SEM (Zeiss Merlin and Zeiss Supra). Both surfaces, facing the separator and the current collector, have been investigated by SEM analysis. The surface facing the separator is exposed by removing the separator from the electrode. The surface facing the current collector is obtained by removing the aluminum foil with a tweezer after having the surface of the cathode attached to a carbon base, as shown in Figure S1. The element distribution in the selected cathode is tested by EDX (Bruker/Quantax 400 detector). An advanced XRD device (STOE Stadi P) is used for the structural characterization of both the cathode and anode. *In situ* XRD experiments are performed for the cathode half-cells in transmission geometry with cells having a special Kapton window to allow for beam transmission.<sup>54</sup> The cell is cycled at a current rate of 0.124 mA between 3 and 4.25 V using a  $\mu\text{AUTOLAB III/FRA2}$  potentiostat. The *in situ* XRD patterns are collected by the STOE diffractometer with Ag  $K\alpha_1$  source ( $\lambda = 0.5594 \text{ \AA}$ ) at room temperature for 20 min for each pattern. The  $2\theta$  scan range for the *in situ* XRD experiment is set from  $0^\circ$  to  $36.6^\circ$  with an angular resolution of  $0.015^\circ$ . *In situ* TR-XRD was performed for the cathode materials in a full de-lithiated state between 25°C and 650°C (25°C, 50°C, and then at 50°C increments up to 650°C). To achieve the fully de-lithiated cathode, the cathode half-cells are assembled followed by a full charge up to 4.25 V with a constant current rate of 0.824 mA and a holding voltage (4.25 V) until the current decreases to 0.1 mA. Then, the cell is opened and the cathode material is extracted from the aluminum current collector, manually hand milled, and filled into a 0.5-mm  $\varnothing$  quartz capillary inside a glove box. The  $2\theta$  scan range for *in situ* XRD experiments is from  $6^\circ$  to  $60.6^\circ$ . The *in situ* TR-XRD patterns are collected using the STOE diffractometer with Mo  $K\alpha_1$  radiation ( $\lambda = 0.7093 \text{ \AA}$ ) for 100 min for each pattern. The *ex situ* XRD tests are performed for the as-opened anode materials at room temperature with an STOE diffractometer with Mo  $K\alpha_1$  radiation. The measurements are carried out between  $4^\circ$  and  $62^\circ$  with an angular resolution of  $0.015^\circ$ .

### Voltage identification method

The DV analysis hypothesizes that the loss of lithium and active material leads to the voltage curve shrinking and shifting. Thus, the specific process shown in Figure 3D is achieved by adjusting the horizontal coordinate as follows:  $n = [0, 1, 2 \dots]$ , where  $n$  is the number of cycles for each cell.  $X_n = [x1_n, x2_n, x3_n, U_{\text{relax}_n}, C_{\text{real}_n}]$  is the

dataset of the  $n^{\text{th}}$  cycle for each cell.  $x1_n$  is the ratio of the shortening of L1 in the  $n^{\text{th}}$  cycle compared with the L1 at the BoL, and can be expressed as:

$$x1_n = \frac{L1_n}{L1_{bol}} \quad (\text{Equation 1})$$

where  $L1_n$  is the length of L1 in the  $n^{\text{th}}$  cycle and  $L1_{bol}$  is the length of L1 at the BoL.

The horizontal coordinate of the cathode OCV curve in the  $n^{\text{th}}$  cycle is shortened to the original  $x1_n$  since the shortening of L1 represents the loss of active material for the cathode and assumes that L1 and loss of the cathode active material are linearly related. The cathode OCV curve at the BoL is noted as  $Uca_{bol}(\text{capacity}, U)$ , thus, the cathode OCV curve in  $n^{\text{th}}$  cycle  $Uca_n$  can be written as:

$$Uca_n = Uca_{bol}(\text{capacity} \times x1_n, U) \quad (\text{Equation 2})$$

Similarly,  $x2_n$  is the ratio of the contraction of L2, and can be written as:

$$x2_n = \frac{L2_n}{L2_{bol}} \quad (\text{Equation 3})$$

where  $L2_n$  is the length of L2 in the  $n^{\text{th}}$  cycle and  $L2_{bol}$  is the length of L2 at the BoL. The horizontal coordinate of the anode OCV curve in  $n^{\text{th}}$  cycle will be shortened to the original  $x2_n$  due to the anode LAM. A translation of the anode OCV curve is caused by LLI during cycling.  $x3_n$  is the shift of the relative voltage windows for the cathode and anode curves, and it can be obtained as:

$$x3_n = L3_n - L3_{bol} + L3_{bol} * (1 - x2_n), \quad (\text{Equation 4})$$

where  $L3_n$  is the length of L3 in the  $n^{\text{th}}$  cycle and  $L3_{bol}$  is the length of L3 at the BoL.  $L3_n - L3_{bol}$  is the change of L3, which is caused by the shortening and shift of the anode OCV curve. Thus, the shortening term  $L3_{bol} * (1 - x2_n)$  is added to  $L3_n - L3_{bol}$  as compensation. The anode OCV curve at BoL is noted as  $Uan_{bol}(\text{capacity}, U)$ , thus, the anode OCV curve in  $n^{\text{th}}$  cycle  $Uan_n$  can be written as:

$$Uan_n = Uan_{bol}(\text{capacity} \times x2_n + x3_n, U) \quad (\text{Equation 5})$$

The full cell OCV curve  $Un$  at the  $n^{\text{th}}$  cycle can be expressed as:

$$Un = Uca_n - Uan_n \quad (\text{Equation 6})$$

When the relaxation voltage  $Urelax_n$  is equal to the  $U$  of  $Un(\text{capacity}, U)$ , and anode OCV, that is, cathode vs.  $\text{Li}^+/\text{Li}$  and anode vs.  $\text{Li}^+/\text{Li}$  in  $n$  cycle is calculated according to Equations 1, 2, 3, 4, 5, and 6.

## SUPPLEMENTAL INFORMATION

Supplemental information can be found online at <https://doi.org/10.1016/j.xcrp.2023.101464>.

## ACKNOWLEDGMENTS

J.Z. would like to thank the foundation of the National Natural Science Foundation of China (NSFC, grant no. 52107230). H.D. would like to thank the foundation of the NSFC (grant no. U20A20310). This work is supported in the frame of the Alexander von Humboldt Postdoctoral Research Program, Fundamental Research Funds for the Central Universities, and Major State Basic Research Development Program of China (973 Program, grant nos. 2022YFB2502304 and 2022YFB2502302). This research contributes to the research performed at the Center for Electrochemical Energy Storage Ulm-Karlsruhe (CELEST).

## AUTHOR CONTRIBUTIONS

Conceptualization, J.Z. and W.X.; methodology, J.Z. and H.D.; investigation, J.Z., W.X., M.K., M.S.D.D., L.M., P.S., W.H., and X.L.; writing – original draft, W.X. and J.Z.; writing – review & editing, J.Z.; resources, H.D., X.W., and H.E.; supervision, M.K., X.W., H.D., and H.E.

## DECLARATION OF INTERESTS

The authors declare no competing interests.

Received: February 21, 2023

Revised: April 28, 2023

Accepted: May 31, 2023

Published: June 20, 2023

## REFERENCES

- Larcher, D., and Tarascon, J.M. (2015). Towards greener and more sustainable batteries for electrical energy storage. *Nat. Chem.* 7, 19–29. <https://doi.org/10.1038/nchem.2085>.
- Kwade, A., Haselrieder, W., Leithoff, R., Modlinger, A., Dietrich, F., and Droeder, K. (2018). Current status and challenges for automotive battery production technologies. *Nat. Energy* 3, 290–300. <https://doi.org/10.1038/s41560-018-0130-3>.
- Hu, X., Xu, L., Lin, X., and Pecht, M. (2020). Battery lifetime prognostics. *Joule* 4, 310–346. <https://doi.org/10.1016/j.joule.2019.11.018>.
- Waag, W., Käbitz, S., and Sauer, D.U. (2013). Experimental investigation of the lithium-ion battery impedance characteristic at various conditions and aging states and its influence on the application. *Appl. Energy* 102, 885–897. <https://doi.org/10.1016/j.apenergy.2012.09.030>.
- Zhu, J., Wang, Y., Huang, Y., Bhushan Gopaluni, R., Cao, Y., Heere, M., Mühlbauer, M.J., Mereacre, L., Dai, H., Liu, X., et al. (2022). Data-driven capacity estimation of commercial lithium-ion batteries from voltage relaxation. *Nat. Commun.* 13, 2261.
- Jin, S., Huang, X., Sui, X., Wang, S., Teodorescu, R., and Stroe, D.I. (2021). Overview of methods for battery lifetime extension. In *23rd European Conference on Power Electronics and Applications (EPE'21 ECCE Europe)*, Ghent, Belgium, 2021, pp. 1–8.
- Harper, G., Sommerville, R., Kendrick, E., Driscoll, L., Slater, P., Stolkin, R., Walton, A., Christensen, P., Heidrich, O., Lambert, S., et al. (2019). Recycling lithium-ion batteries from electric vehicles. *Nature* 575, 75–86.
- Woody, M., Arbabzadeh, M., Lewis, G.M., Keoleian, G.A., and Stefanopoulou, A. (2020). Strategies to limit degradation and maximize Li-ion battery service lifetime - critical review and guidance for stakeholders. *J. Energy Storage* 28, 101231. <https://doi.org/10.1016/j.est.2020.101231>.
- Bresser, D., Hosoi, K., Howell, D., Li, H., Zeisel, H., Amine, K., and Passerini, S. (2018). Perspectives of automotive battery R&D in China, Germany, Japan, and the USA. *J. Power Sources* 382, 176–178. <https://doi.org/10.1016/j.jpowsour.2018.02.039>.
- Kim, U.-H., Park, G.-T., Son, B.-K., Nam, G.W., Liu, J., Kuo, L.-Y., Kaghazchi, P., Yoon, C.S., and Sun, Y.-K. (2020). Heuristic solution for achieving long-term cycle stability for Ni-rich layered cathodes at full depth of discharge. *Nat. Energy* 5, 860–869. <https://doi.org/10.1038/s41560-020-00693-6>.
- Odziomek, M., Chaput, F., Rutkowska, A., Świerczek, K., Olszewska, D., Sitarz, M., Lerouge, F., and Parola, S. (2017). Hierarchically structured lithium titanate for ultrafast charging in long-life high capacity batteries. *Nat. Commun.* 8, 15636. <https://doi.org/10.1038/ncomms15636>.
- Palanisamy, M., Parekh, M.H., and Pol, V.G. (2020). In situ replenishment of formation cycle lithium-ion loss for enhancing battery life. *Adv. Funct. Mater.* 30, 2003668. <https://doi.org/10.1002/adfm.202003668>.
- Wang, C.-Y., Liu, T., Yang, X.-G., Ge, S., Stanley, N.V., Rountree, E.S., Leng, Y., and McCarthy, B.D. (2022). Fast charging of energy-dense lithium-ion batteries. *Nature* 611, 485–490.
- Xing, Y., Ma, E.W.M., Tsui, K.L., and Pecht, M. (2011). Battery management systems in electric and hybrid vehicles. *Energies* 4, 1840–1857.
- Dai, H., Jiang, B., Hu, X., Lin, X., Wei, X., and Pecht, M. (2021). Advanced battery management strategies for a sustainable energy future: multilayer design concepts and research trends. *Renew. Sustain. Energy Rev.* 138, 110480.
- Darma, M.S.D., Lang, M., Kleiner, K., Mereacre, L., Liebau, V., Fauth, F., Bergfeldt, T., and Ehrenberg, H. (2016). The influence of cycling temperature and cycling rate on the phase specific degradation of a positive electrode in lithium ion batteries: a post mortem analysis. *J. Power Sources* 327, 714–725.
- Dolotko, O., Senyshyn, A., Mühlbauer, M.J., Nikolowski, K., Scheiba, F., and Ehrenberg, H. (2012). Fatigue process in Li-ion Cells: an in situ combined neutron diffraction and electrochemical study. *J. Electrochem. Soc.* 159, A2082–A2088.
- Zhang, G., Wei, X., Han, G., Dai, H., Zhu, J., Wang, X., Tang, X., and Ye, J. (2021). Lithium plating on the anode for lithium-ion batteries during long-term low temperature cycling. *J. Power Sources* 484, 229312.
- Darma, M.S.D., Zhu, J., Yan, P., Zheng, C., Mühlbauer, M.J., Sørensen, D.R., Indris, S., Bergfeldt, T., Das, C., Heere, M., et al. (2021). Managing life span of high-energy LiNi<sub>0.88</sub>Co<sub>0.11</sub>Al<sub>0.01</sub>O<sub>2</sub>[C–Si Li-ion batteries. *ACS Appl. Energy Mater.* 4, 9982–10002. <https://doi.org/10.1021/acsaem.1c01946>.
- Sørensen, D.R., Heere, M., Zhu, J., Darma, M.S.D., Zimnik, S., Mühlbauer, M., Mereacre, L., Baran, V., Senyshyn, A., and Knapp, M. (2020). Fatigue in high-energy commercial Li-batteries while cycling at standard conditions. An in-situ neutron powder diffraction study. *ACS Appl. Energy Mater.* 3, 6611–6622.
- Zhu, J., Su, P., Dewi Darma, M.S., Hua, W., Mereacre, L., Liu-Théato, X., Heere, M., Sørensen, D.R., Dai, H., Wei, X., et al. (2022). Multiscale investigation of discharge rate dependence of capacity fade for lithium-ion battery. *J. Power Sources* 536, 231516.
- Aiken, C.P., Logan, E.R., Eldesoky, A., Hebecker, H., Oxner, J.M., Harlow, J.E., Metzger, M., and Dahn, J.R. (2022). Li [Ni<sub>0.5</sub>Mn<sub>0.3</sub>Co<sub>0.2</sub>]O<sub>2</sub> as a superior alternative to LiFePO<sub>4</sub> for long-lived low voltage Li-ion cells. *J. Electrochem. Soc.* 169, 050512. <https://doi.org/10.1149/1945-7111/ac67b5>.
- German, F., Hintennach, A., LaCroix, A., Thiemi, D., Oswald, S., Scheiba, F., Hoffmann, M.J., and Ehrenberg, H. (2014). Influence of temperature and upper cut-off voltage on the formation of lithium-ion cells. *J. Power Sources* 264, 100–107. <https://doi.org/10.1016/j.jpowsour.2014.04.071>.
- Zhu, J., Knapp, M., Sørensen, D.R., Heere, M., Darma, M.S., Müller, M., Mereacre, L., Dai, H., Senyshyn, A., Wei, X., and Ehrenberg, H. (2021). Investigation of capacity fade for 18650-type lithium-ion batteries cycled in different state of charge (SoC) ranges. *J. Power Sources* 489, 229422.
- Gao, Y., Jiang, J., Zhang, C., Zhang, W., and Jiang, Y. (2018). Aging mechanisms under different state-of-charge ranges and the

- multi-indicators system of state-of-health for lithium-ion battery with Li (NiMnCo) O<sub>2</sub> cathode. *J. Power Sources* 400, 641–651.
26. Matsuda, T., Ando, K., Myojin, M., Matsumoto, M., Sanada, T., Takao, N., Imai, H., and Imamura, D. (2019). Investigation of the influence of temperature on the degradation mechanism of commercial nickel manganese cobalt oxide-type lithium-ion cells during long-term cycle tests. *J. Energy Storage* 21, 665–671. <https://doi.org/10.1016/j.est.2019.01.009>.
  27. Wang, J., Purewal, J., Liu, P., Hicks-Garner, J., Soukazian, S., Sherman, E., Sorenson, A., Vu, L., Tataria, H., and Verbrugge, M.W. (2014). Degradation of lithium ion batteries employing graphite negatives and nickel–cobalt–manganese oxide+ spinel manganese oxide positives: Part 1, aging mechanisms and life estimation. *J. Power Sources* 269, 937–948. <https://doi.org/10.1016/j.jpowsour.2014.07.030>.
  28. Wong, D., Shrestha, B., Wetz, D.A., and Heinzl, J.M. (2015). Impact of high rate discharge on the aging of lithium nickel cobalt aluminum oxide batteries. *J. Power Sources* 280, 363–372.
  29. Mussa, A.S., Liivat, A., Marzano, F., Klett, M., Philippe, B., Tengstedt, C., Lindbergh, G., Edström, K., Lindström, R.W., and Svens, P. (2019). Fast-charging effects on ageing for energy-optimized automotive LiNi<sub>1</sub>/3Mn<sub>1</sub>/3Co<sub>1</sub>/3O<sub>2</sub>/graphite prismatic lithium-ion cells. *J. Power Sources* 422, 175–184. <https://doi.org/10.1016/j.jpowsour.2019.02.095>.
  30. Omar, N., Monem, M.A., Firouz, Y., Salminen, J., Smekens, J., Hegazy, O., Gaulous, H., Mulder, G., Van den Bossche, P., Coosemans, T., and Van Mierlo, J. (2014). Lithium iron phosphate based battery – assessment of the aging parameters and development of cycle life model. *Appl. Energy* 113, 1575–1585. <https://doi.org/10.1016/j.apenergy.2013.09.003>.
  31. Zhu, J., Su, P., Dewi Darma, M.S., Hua, W., Mereacre, L., Liu-Théato, X., Heere, M., Sørensen, D.R., Dai, H., Wei, X., et al. (2022). Multiscale investigation of discharge rate dependence of capacity fade for lithium-ion battery. *J. Power Sources* 536, 231516. <https://doi.org/10.1016/j.jpowsour.2022.231516>.
  32. Zhu, Y., Yan, F., Kang, J., Du, C., Zhang, C., and Turkson, R.F. (2017). Fading analysis of the Li (NiCoMn) O<sub>2</sub> battery under different SOC cycle intervals. *Ionics* 23, 1383–1390.
  33. Ecker, M., Nieto, N., Käbitz, S., Schmalstieg, J., Blanke, H., Warnecke, A., and Sauer, D.U. (2014). Calendar and cycle life study of Li (NiMnCo) O<sub>2</sub>-based 18650 lithium-ion batteries. *J. Power Sources* 248, 839–851.
  34. Bharathraj, S., Adiga, S.P., Mayya, K.S., Song, T., Kim, J., and Sung, Y. (2020). Degradation-guided optimization of charging protocol for cycle life enhancement of Li-ion batteries with Lithium Manganese Oxide-based cathodes. *J. Power Sources* 474, 228659. <https://doi.org/10.1016/j.jpowsour.2020.228659>.
  35. Chen, J., Yang, Y., Tang, Y., Wang, Y., Li, H., Xiao, X., Wang, S., Darma, M.S.D., Etter, M., Missyul, A., et al. (2022). Constructing a thin disordered self-protective layer on the LiNiO<sub>2</sub> primary particles against oxygen release. *Adv. Funct. Mater.* 33, 2211515. <https://doi.org/10.1002/adfm.202211515>.
  36. Rodríguez-Carvajal, J. (1993). Recent advances in magnetic-structure determination by neutron powder diffraction. *Physica B* 192, 55–69. [https://doi.org/10.1016/0921-4526\(93\)90108-1](https://doi.org/10.1016/0921-4526(93)90108-1).
  37. Zhu, J., Dewi Darma, M.S., Knapp, M., Sørensen, D.R., Heere, M., Fang, Q., Wang, X., Dai, H., Mereacre, L., Senyshyn, A., et al. (2020). Investigation of lithium-ion battery degradation mechanisms by combining differential voltage analysis and alternating current impedance. *J. Power Sources* 448, 227575.
  38. Liu, X., Xu, G.L., Yin, L., Hwang, I., Li, Y., Lu, L., Xu, W., Zhang, X., Chen, Y., Ren, Y., et al. (2020). Probing the thermal-driven structural and chemical degradation of Ni-rich layered cathodes by Co/Mn exchange. *J. Am. Chem. Soc.* 142, 19745–19753. <https://doi.org/10.1021/jacs.0c09961>.
  39. Nam, K.-W., Bak, S.-M., Hu, E., Yu, X., Zhou, Y., Wang, X., Wu, L., Zhu, Y., Chung, K.-Y., and Yang, X.-Q. (2013). Combining in situ synchrotron X-ray diffraction and absorption techniques with transmission electron microscopy to study the origin of thermal instability in overcharged cathode materials for lithium-ion batteries. *Adv. Funct. Mater.* 23, 1047–1063. <https://doi.org/10.1002/adfm.201200693>.
  40. Zhang, Y., and Wang, C.-Y. (2009). Cycle-life characterization of automotive lithium-ion batteries with LiNiO<sub>2</sub> cathode. *J. Electrochem. Soc.* 156, A527–A535.
  41. Stiaszny, B., Ziegler, J.C., Krauß, E.E., Schmidt, J.P., and Ivers-Tiffée, E. (2014). Electrochemical characterization and post-mortem analysis of aged LiMn<sub>2</sub>O<sub>4</sub>-Li (NiO, 5MnO, 3CoO, 2) O<sub>2</sub>/graphite lithium ion batteries. Part I: cycle aging. *J. Power Sources* 251, 439–450.
  42. Stiaszny, B., Ziegler, J.C., Krauß, E.E., Zhang, M., Schmidt, J.P., and Ivers-Tiffée, E. (2014). Electrochemical characterization and post-mortem analysis of aged LiMn<sub>2</sub>O<sub>4</sub>-NMC/graphite lithium ion batteries part II: calendar aging. *J. Power Sources* 258, 61–75.
  43. Surace, Y., Leanza, D., Mirolo, M., Kondracki, Ł., Vaz, C.A.F., El Kazzi, M., Novák, P., and Trabesinger, S. (2022). Evidence for stepwise formation of solid electrolyte interphase in a Li-ion battery. *Energy Storage Mater.* 44, 156–167. <https://doi.org/10.1016/j.ensm.2021.10.013>.
  44. Vekilov, P.G. (2010). Nucleation. *Cryst. Growth Des.* 10, 5007–5019. <https://doi.org/10.1021/cg1011633>.
  45. Schuster, S.F., Bach, T., Fleder, E., Müller, J., Brand, M., SEXTL, G., and Jossen, A. (2015). Nonlinear aging characteristics of lithium-ion cells under different operational conditions. *J. Energy Storage* 1, 44–53. <https://doi.org/10.1016/j.est.2015.05.003>.
  46. Wang, J., Purewal, J., Liu, P., Hicks-Garner, J., Soukazian, S., Sherman, E., Sorenson, A., Vu, L., Tataria, H., and Verbrugge, M.W. (2014). Degradation of lithium ion batteries employing graphite negatives and nickel–cobalt–manganese oxide + spinel manganese oxide positives: Part 1, aging mechanisms and life estimation. *J. Power Sources* 269, 937–948. <https://doi.org/10.1016/j.jpowsour.2014.07.030>.
  47. Keil, P., and Jossen, A. (2016). Calendar aging of NCA lithium-ion batteries investigated by differential voltage analysis and coulomb tracking. *J. Electrochem. Soc.* 164, A6066–A6074. <https://doi.org/10.1149/2.0091701jes>.
  48. Flügel, M., Kasper, M., Pfeifer, C., Wohlfahrt-Mehrens, M., and Waldmann, T. (2021). Cu dissolution during over-discharge of Li-ion cells to 0 V: A post-mortem study. *J. Electrochem. Soc.* 168, 020506. <https://doi.org/10.1149/1945-7111/abcd5f>.
  49. Fear, C., Juarez-Robles, D., Jeevarajan, J.A., and Mukherjee, P.P. (2018). Elucidating copper dissolution phenomenon in Li-ion cells under overdischarge extremes. *J. Electrochem. Soc.* 165, A1639–A1647. <https://doi.org/10.1149/2.0671809jes>.
  50. Jung, R., Linsenmann, F., Thomas, R., Wandt, J., Solchenbach, S., Maglia, F., Stinner, C., Tromp, M., and Gasteiger, H.A. (2019). Nickel, manganese, and cobalt dissolution from Ni-rich NMC and their effects on NMC622-graphite cells. *J. Electrochem. Soc.* 166, A378–A389. <https://doi.org/10.1149/2.1151902jes>.
  51. Zech, C., Evertz, M., Börner, M., Kayser, Y., Hönicke, P., Winter, M., Nowak, S., and Beckhoff, B. (2021). Quantitative manganese dissolution investigation in lithium-ion batteries by means of X-ray spectrometry techniques. *J. Anal. At. Spectrom.* 36, 2056–2062. <https://doi.org/10.1039/d0ja00491j>.
  52. Sørensen, D.R., Heere, M., Zhu, J., Darma, M.S.D., Zimmnik, S.M., Mühlbauer, M.J., Mereacre, L., Baran, V., Senyshyn, A., Knapp, M., and Ehrenberg, H. (2020). Fatigue in high-energy commercial Li batteries while cycling at standard conditions: an in situ neutron powder diffraction study. *ACS Appl. Energy Mater.* 3, 6611–6622.
  53. Zhu, J., Knapp, M., Sørensen, D.R., Heere, M., Darma, M.S., Müller, M., Mereacre, L., Dai, H., Senyshyn, A., Wei, X., and Ehrenberg, H. (2021). Investigation of capacity fade for 18650-type lithium-ion batteries cycled in different state of charge (SoC) ranges. *J. Power Sources* 489, 229422. <https://doi.org/10.1016/j.jpowsour.2020.229422>.
  54. Sharma, P., Das, C., Indris, S., Bergfeldt, T., Mereacre, L., Knapp, M., Geckle, U., Ehrenberg, H., and Darma, M.S.D. (2020). Synthesis and characterization of a multication doped Mn spinel, LiNi<sub>0.3</sub>Cu<sub>0.1</sub>Fe<sub>0.2</sub>Mn<sub>1.0</sub>O<sub>4</sub>, as 5 V positive electrode material. *ACS Omega* 5, 22861–22873.